Au/ZSM-5 catalyses the selective oxidation of CH$_4$ to CH$_3$OH and CH$_3$COOH using O$_2$

Guodong Qi[1], Thomas E. Davies[2], Ali Nasrallah[2], Mala A. Sainna[2], Alexander G. R. Howe[3], Richard J. Lewis[2], Matthew Quesne[2], C. Richard A. Catlow[2], David J. Willock[2], Qian He[3], Donald Bethell[2], Mark J. Howard[2], Barry A. Murrer[2], Brian Harrison[2], Christopher J. Kiely[4], Xingling Zhao[1], Feng Deng[1], Jun Xu[1]* and Graham J. Hutchings[2]*

[1] National Centre for Magnetic Resonance in Wuhan, State Key Laboratory of Magnetic Resonance and Atomic and Molecular Physics, Innovation Academy for Precision Measurement Science and Technology, Chinese Academy of Sciences, Wuhan 430071, China. University of Chinese Academy of Sciences, Beijing 100049, China

[2] Max Planck–Cardiff Centre on the Fundamentals of Heterogeneous Catalysis FUNCAT, Cardiff Catalysis Institute, School of Chemistry, Cardiff University, Main Building, Park Place, Cardiff, CF10 3AT, UK.

[3] National University of Singapore, Singapore 117575, Singapore

[4] Department of Materials Science and Engineering, Lehigh University, 5 East Packer Avenue, Bethlehem, Pennsylvania, PA 18015, USA.

*Hutch@cardiff.ac.uk; xujun@wipm.ac.cn

Abstract

The oxidation of methane, the main component of natural gas, to selectively form oxygenated chemical feedstocks using molecular oxygen has been a long-standing grand challenge in catalysis. Here, using gold nanoparticles supported on the zeolite ZSM-5 we introduce a method to oxidise methane to methanol and acetic acid in water at temperatures between 120-240 °C using molecular oxygen in the absence of any added co-reductant. Electron microscopy reveals that the catalyst does not contain gold atoms or clusters, but rather gold nanoparticles are the active component while a mechanism involving surface adsorbed species is proposed in which methanol and acetic acid are formed via parallel pathways.

Introduction

The direct selective oxidation of CH_4 to chemical intermediates using molecular oxygen is challenging since over-oxidation by combustion to CO_2 and H_2O is thermodynamically preferred. Commercially, CH_4 is converted into chemicals using an indirect route involving the production of synthesis gas $(CO + H_2)$[1]. However, the direct route has been the subject of intense interest for many decades[2,3]. Early studies focused on using gas phase reactions at moderate temperatures (400-500 °C) and oxygenated products can be observed if the temperature and the O_2 partial pressure are carefully controlled[4]. There have been many approaches to this challenge where the emphasis has been on using lower temperature to enable improved selectivity to oxygenated products, but often these involve catalytic cycles that are not closed. For example, Periana and co-workers reported that electrophilic Hg and Pt-complexes can oxidise methane in oleum[5,6], forming methyl hydrogen sulfate which has to be hydrolyzed separately to release methanol and SO_2.

Most recent interest has centred on metal-exchanged zeolite catalysts. Fe-ZSM-5 was shown to form CH_3OH with N_2O as oxidant[7-10], FeCu-ZSM-5 forms CH_3OH in high selectivity using H_2O_2 as oxidant[11,12], Cu-mordenite[13] and Rh-ZSM-5[14,15] both can form CH_3OH with O_2 using CO as a co-reductant. Nanoparticulate AuPd alloys supported on ZSM-5 are also active with in situ formed H_2O_2[16] and unsupported AuPd alloys are active with H_2O_2[17]. For all these catalysts no selective oxygenate products are formed with O_2 alone. A detailed comparison of recently reported catalysts is presented in Supplementary Tables 1 and 2.

Cu-mordenite catalysts when operated in a two stage non-closed catalytic cycle can form CH_3OH[18-20]. An oxidised Cu species is reacted with CH_4 to form a surface methoxyl which is subsequently extracted at a lower temperature with water. van Bokhoven and co-workers demonstrated[21] that Cu-mordenite can oxidise CH_4 with a continuous flow of H_2O to produce methanol; however, this reaction is stoichiometric rather than catalytic as the turnover is 0.21 mol CH_3OH/mol Cu. Román-Leshkov and co-workers[22,23] have shown that Cu-H-ZSM-5 can oxidise methane in a continuous flow of H_2O and O_2 and can achieve a closed catalytic cycle with low conversion and the turnover number (TON) is 1.4 after a long reaction time of 288 h. Most recently Koishybay and Shantz[24] have shown that for methane oxidation catalysed with Cu-SSZ-13 under similar reaction conditions H_2O is the source of the oxygen in the CH_3OH product, but the yields are still very low. There is therefore a need to identify improved catalysts for the methane oxidation reaction.

Here we report that the oxidation of CH_4 using O_2 can be achieved in the absence of a co-reductant (H_2 or CO) in a closed catalytic cycle using Au supported on ZSM-5 with high selectivity to oxygenated products at 120-240 °C and with low CO_2 production.

Results

Catalyst preparation and methane oxidation using Au/ZSM-5

We prepared Au catalysts supported on ZSM-5 using a deposition precipitation method. The characterised catalysts (Supplementary Figs 1, 2 and Supplementary Table 3) were used for the direct oxidation of CH_4 with O_2 in water for 2 h at 240 °C with 3.5 bar O_2 and 20.7 bar CH_4 charged at room temperature (Table 1). It was observed that oxygenated products could be formed, in contrast to earlier studies where the presence of a co-reductant was necessary[14]. Under these conditions, methanol, methyl hydroperoxide, acetic acid and peracetic acid were detected using quantitative nuclear magnetic resonance (NMR) analysis (Supplementary Figs 3 and 4)[16,17]. Significantly, there was no ^{1}H NMR evidence of formaldehyde (hydrate), its methyl hemiacetal, or of formic acid among the liquid products (Supplementary Fig. 3). The optimum final pH used in the deposition precipitation for catalyst preparation was determined to be pH 6-8 (Supplementary Figure 5) and, in all following experiments, catalysts were prepared at pH 6. We contrasted the use of ZSM-5 as a support for Au, with that of silica and alumina (Table 1 - entries 2-4, Supplementary Fig. 6). Au-ZSM-5 showed the best activity while H-ZSM-5 itself showed much lower activity and selectivity in the absence of Au (Table 1 - entry 1, Supplementary Table 4) despite the presence of Fe in the zeolite samples (Supplementary Table 3).

The Si/Al ratio of the ZSM-5 was found to affect the catalytic performance indicating the acidity of the support is of importance. ZSM-5 was sourced from two commercial suppliers both giving similar results (Supplementary Table 5). The highest productivity was obtained with the ZSM-5 material having the lowest Si/Al ratio (23). The topology of the structure also appears to be important; Zeolite Y with a very low Si/Al ratio of 2.8 is less effective than any ZSM-5 support and a MOR material with a very similar Si/Al ratio has only half the productivity value. This is consistent with the relative proton mobility in these materials which follows the order H-ZSM-5 > H-MOR > H-Y.**Error! Reference source not found.** Au loading was investigated (Supplementary Figure 7) and the yield of oxygenated products increased with the amount of Au present. Furthermore, X-ray photoelectron spectroscopy showed that all catalysts contain largely Au^0 with some cationic Au possibly present at very low Au loading (Supplementary Figure 2). The effect of O_2 partial pressure was also investigated (Fig. 1a-d).

For low O_2 partial pressures the formation of the selective oxygenated products was noted with low CO_2 generation (Table 1, entries 4,5,7). Use of short reaction times (Figure 1e-h) showed that the over-oxidation to CO_2 could be decreased (Table 1, entries 4 and 9) giving almost complete selectivity to oxygenated products. Most importantly, when using low Au loading (0.25 wt.% Au/ZSM-5) the over-oxidation to CO_2 can be decreased to below the limit of detection (Table 1, entries 8 and 10). Lowering the temperature of reaction was also found to improve oxygenate selectivity (Supplementary Figure 8). Methane oxidation could still be observed at temperatures as low as 120 °C although the overall product yield was reduced. When using synthetic air under the equivalent reaction conditions, similar results were obtained (Supplementary Table 6) with an estimated TON of 93 based on estimated surface Au atom number (Supplementary Note 1, value based on Supplementary Table 6, entry 2). Therefore, it is clear that the catalytic oxidation of CH_4 with O_2 using Au/ZSM-5 is being achieved without the need for a co-reductant and is capable of appreciable rates (Supplementary Table 6). The catalysed reaction continues over the 2 h reaction time we have investigated (Figure 1e-h). Catalyst reuse (Supplementary Figure 9) showed that there is a small loss of activity after the first run with an increased selectivity to acetic acid.

These experiments have demonstrated that it is possible for methane to be selectively oxidised to C_1 and C_2 oxygenates using only molecular oxygen as the terminal oxidant in a closed catalytic cycle with significant turnover numbers. This finding can be considered to be a proof-of-concept study as methane conversions are indeed low (Supplementary Table 7) and the products that are formed are very dilute in an aqueous solution. To increase conversion, reactions at lower methane partial pressure were caried out and we achieved methane conversions of up to 4.6 % (Figure 2, Supplementary Table 7) whilst maintaining a reasonable oxygenate selectivity. At these higher conversions the products are mainly C_2 oxygenates.

Catalyst characterisation

A sub-set of the materials were characterised using aberration-corrected scanning transmission electron microscopy (AC-STEM), which has sufficient spatial resolution and sensitivity to identify Au species ranging from nanoparticles to sub-nm clusters to isolated atoms or cations[26,27]. Previous work by Shan *et al.* on atomically dispersed Rh catalysts[14,15] and Jin *et al.* on supported Ir-cluster catalysts[28] clearly demonstrated the importance of isolated cations or sub -nm clusters for activating methane. Interestingly, only Au nanoparticles greater than 3 nm diameter (*i.e.*, larger than the zeolite micropores) were found in both the fresh and used 0.5

wt.% Au/ZSM-5 catalysts (Figure 3 and Supplementary Fig. 10) and no sub-nm Au clusters or isolated Au atoms were detected, even for catalysts employed in multiple reuse tests (Supplementary Figure 11). ZSM-5 is known to contain Fe impurities within the porous structure[11] and as the Au nanoparticles are on the exterior surface of the ZSM-5 crystallites there is no possibility of any interaction between Au and Fe playing a role in the observed catalysis. Au particle size distributions were determined from bright-field TEM images (Supplementary Figure 12) and a modest increase in average particle size from 8.1 nm to 11.7-14.1 nm was found after reaction times of 2 h and 4 h. The averages seen post reaction are within the error limits of the particle size distribution (PSD). Additional AC-STEM experiments for catalysts after three 2 h reactions carried out for the reuse studies gave a PSD with a mean particle diameter of 9.8 nm (Supplementary Figure 11d), indicating that there is little or no sintering of Au particles under reaction conditions or the conditions used for catalyst regeneration. Consistent particle size distributions were also observed from SEM back-scattered electron imaging, which provides a larger field of view of the sample compared to TEM/STEM analysis. Lowering the Au loading on ZSM-5 (Supplementary Figure 13) from 0.5 wt.% to 0.25 wt.% and even 0.12 wt.% still resulted in Au nanoparticles having a similar mean size, but lower number densities, whereas increasing the Au loading to 1 wt.% caused significant agglomeration of the Au. We therefore infer that the active species for methane oxidation are the Au nanoparticles.

Fresh and used Au/ZSM-5 samples were also characterized using ^{27}Al MAS NMR, which only showed signals consistent with Al^{3+} in the tetrahedral framework sites of the zeolite (Supplementary Figure 14). This indicates that octahedrally coordinated, extra-framework Al^{3+} is not present in these materials and that dealumination of the zeolite does not occur under our reaction conditions.

Computational and mechanistic studies

We have explored the activation of oxygen and methane using DFT calculations (PBE+D3) with models covering periodic slabs representing stepped surfaces on large particles, Au_{38} nanoparticles and an Au^+ extra-framework cation, Au^+/ZSM-5 (Supplementary Figure 15). For all structures, adsorption of oxygen is accompanied by electron donation from the metal to produce an O_2^* surface bound superoxo species. Figure 4 shows that, on the Au_{38} nanoparticle superoxo dissociation to atomic oxygen, $2O^*$, involves a barrier of only 39 kJ mol^{-1}, while using the stepped slab model this is somewhat higher (84 kJ mol^{-1}). Even so, it is clear that the larger

nanoparticles observed in our electron microscopy studies should be able to promote the dissociation of oxygen under our experimental conditions. In contrast, extra-framework cationic gold, $Au^{2+}O_2$/ZSM-5, whilst strongly activating O_2, lacks an adjacent redox centre to bind the distal oxygen. This means that $Au^{3+}O$/ZSM-5 formation can only proceed via hydrogen abstraction from CH_4 which is blocked by a prohibitively high barrier (~140 kJ mol^{-1}, Supplementary Note 2, Supplementary Figure 16). Under our experimental conditions superoxo dissociation may also be facilitated through protonation of the molecular adsorbate which would be favoured in acidic solution, suggesting one reason for the improved activity seen with H-ZSM-5(25) compared to H-ZSM-5(170) (Supplementary Figure 6 and Supplementary Table 5).

The activation of methane by O_2^{-*} and O^* ([O] in equation 1) was considered for the elementary step:

$$CH_4 + [O] \rightleftharpoons CH_3^* + [O]H \tag{1}$$

Generally, we find that the barrier for O_2^{-*} to activate methane is considerably higher than that for O^* (stepped Au(100)O_2: 124 kJ mol^{-1}, $Au^{2+}O_2$/ZSM-5: 125 kJ mol^{-1}, $Au_{38}O_2$: 57 kJ mol^{-1} *cf* highly stepped Au(100)O: 84 kJ mol^{-1}, $Au_{38}O$: 65 kJ mol^{-1}, Supplementary Figs. 16-19). This suggests that the dissociation of oxygen to form surface oxygen species will lead to easier methane activation to CH_3^* on the surface of Au nanoparticles. Calculations for the activation of CH_4 over highly stepped Au(100) and Au_{38} models by O atoms are compared in Figure 4. This highlights that the barriers involved are lower on particles of the order of 1 nm than for larger particles of the type seen in our microscopy analysis. The 1 nm scale particles also show a higher affinity for oxygen.

From the CH_3^* species produced after initial methane activation further reaction with O_2^* or O^* would be expected to lead to the C_1 products, methyl hydroperoxide and methanol. For example:

$$CH_3^* + O_2^* \rightleftharpoons CH_3OO^* \tag{2}$$

$$CH_3OO^* + H_2O \rightleftharpoons CH_3OOH + OH^* \tag{3}$$

$$CH_3OO^* + H_2O \rightleftharpoons CH_3O* + 2OH^* \tag{4}$$

$$CH_3O^* + H_2O \rightleftharpoons CH_3OH + OH^* \tag{5}$$

More intriguing is the early production of a large amount of C_2 products, acetic acid and

peracetic acid, even in the absence of CO as a co-reductant (*e.g.* Table 1, entries 9 and 10, Figure 5c). It could be envisaged that these arise from ethane contamination of the CH_4 gas or coupling of CH_3^* during the reaction to form ethane and that ethane is oxidised to C_2 products. Analysis confirmed that ethane was not a contaminant of the methane used here and experiments with ethane as the reactant showed the major product to be CO_2 along with acetic acid and some ethanol (Supplementary Table 8). As neither ethane nor ethanol was detected during the reaction of methane (Supplementary Table 9) we concluded that ethane is not a reaction intermediate. Interestingly, methane was also observed as a product from ethane oxidation which we considered due to a reaction of ethane on the zeolite; reacting ethane with ZSM-5 in the absence of Au under the same conditions gave much higher CH_4 yields (Supplementary Tables 8 and 9). The zeolite also has activity for ethane oxidation, but this is enhanced by the presence of Au.

Given that ethane is not the source of C_2 products, we speculate that the intermediates CH_3OO^* (reaction (2)) and CH_3O^*, which lead to the C_1 products following reactions (4) and (5), are also involved in a further cascade of oxidation reactions to create surface bound C_1 species; CH_2O^*, CHO^* and CO^*. These, along with CH_3^*, CH_3O^* and CH_3OO^* would establish a steady state population of C_1 species on the catalyst surface. Reaction of CH_3^* with CO^* is one possible route to a C_2 intermediate which will oxidise to acetic acid before being able to desorb from the catalyst surface. As Au is known to be an active catalyst for methanol carbonylation[29] we also performed experiments using water solvent spiked with methanol at our usual product level (Supplementary Figure 20). However, this demonstrated that methanol does not significantly re-adsorb on the catalyst to take part in the C_2 synthesis pathway under our reaction conditions. The idea of parallel pathways to C_1 and C_2 products led to further kinetic experiments.

Comparison of the temperature dependence of reactions in H_2O and D_2O solvents (Supplementary Table 10) shows that, although the total moles of carbon in the products produced are similar (Supplementary Figure 21a), the behaviour of the C_1 and C_2 product yields are quite different: C_1 products show a similar increase with temperature in both solvents, whereas C_2 yield increases with temperature in H_2O but decreases with temperature in D_2O (Supplementary Figure 21b), with a correspondingly higher production of CO_2 in the deuterated solvent (Supplementary Figure 21a). Considering the effects on product formation of changing from H_2O to D_2O as a function of time (Figure 5, Supplementary Table 11), total

methane conversion shows practically no kinetic isotope effect (KIE, $k_H/k_D = 1.08$, Figure 5a) but this conceals more substantial effects on the separate product streams, especially during the first 60 min. For example, CH_3OH appearance shows $k_H/k_D = 0.42$ during that time (Figure 5b) but the effect diminishes beyond 60 min. For the C_2-oxygenates, there appears to be rapid production within the first 5 min of reaction in both solvents (Figure 5c). Thereafter, production of C_2 products continues in H_2O and this remains a major route to oxygenated products throughout, albeit at a slower rate than during the initial period. In contrast, in D_2O the formation of C_2 oxygenates has finished before 5 min of reaction. Correspondingly, CO_2 production is faster in D_2O than H_2O throughout, $k_H/k_D = 0.81$ (Figure 5d). The complexity of the pattern of behaviour and the changes in KIE with time on-line suggest that several steps may involve water molecules but the KIE magnitudes indicate that none are primary KIEs arising from kinetically significant H-transfer. The largest effects are inverse KIEs, well-known in homogeneous acid-base catalysis; in the present heterogeneous system, desorption of CH_3OH from surface CH_3O^* might be an analogous specific hydrogen-ion catalysed process. Indeed, the low levels of product formed may mean that the adsorptive capacity of the catalyst is significant, and these desorption processes dominate the kinetic measurements. The inverse KIE on CO_2 formation, however, is not explicable in this way; but the very low rate of production of C_2 products in D_2O solvent after the first 5 minutes suggests that the higher rate of CO_2 production in D_2O is linked to differences in the C_2 pathway for the deuterated and normal solvents.

We also note that the routes to methyl hydroperoxide and methanol lead to a net oxidation of the Au nanoparticles as implied by the OH^* remaining after steps (3)-(5). In the absence of a co-reductant, methane, via reaction (1), will also serve to reduce the catalyst surface but is likely to be slow leading to blocking of sites for oxygen activation. Previous studies have shown that CO can be incorporated when added as a co-reductant for the reaction of CH_4 or C_2H_6 with O_2[14,15,28] and in the proposed C_1 pool of surface species CO is key. Accordingly, we have also studied the addition of CO to the reactant stream (Table 1 entries 11 and 12, Supplementary Figure 22 and Supplementary Tables 4, 9 and 12). The catalyst activity was indeed found to be much higher when CO is present with TONs of up to 1400 based on estimated surface Au atom number, indicating that by addition of a co-reductant the catalytic cycle can be accelerated. However, while methanol productivity is increased by an order of magnitude the increase in acetic acid is more modest. The methylhydroperoxy product is no longer observed, which we attribute to reactions of the type:

$$CH_3OO^* + CO \rightleftharpoons CH_3O^* + CO_2 \qquad\qquad (6)$$

The activation barrier for this reaction has been estimated theoretically at 75-80 kJ mol^{-1} in gas and liquid phase[30], and so would require surface catalysis to occur at significant rate in our system. If a partial equilibrium exists between CH_3^* and CH_3OO^*, added CO will also suppress the abundance of CH_3^*, which may explain the smaller increase in C_2 products compared to methanol. However, approximately 8 % of the added CO is oxidised to CO_2, and so its dominant role is likely to be via reduction of the catalyst surface, improving the ability of the catalyst to activate O_2. When CO was present, the fractional increase in the average Au particle size observed by electron microscopy after reaction was notably smaller. After a 4 h reaction with CH_4 (20.7 bar), O_2 (1.0 bar), CO (2.5 bar) the average Au particle size was 11.7 nm (Supplementary Figure 12b) as opposed to 14.1 nm (Supplementary Figure 12c) for post reaction samples when no CO had been added, indicating that the presence of CO may hinder the Au agglomeration process. ^{1}H and ^{13}C NMR spectroscopy shows that the acetic acid formed from the reaction with CO present does not arise from the carbonylation of methanol and so the pathway to acetic acid is not via methanol on Au/ZSM-5 (Supplementary Figs. 23 and 24) even when CO is a co-reactant. The experiments with ^{13}C enriched CH_4 and with ^{13}C enriched CO show that the carbon from methane appears at both positions in the acetic acid product whereas CO almost exclusively enters the carbonyl functional group (Supplementary Table 13), as would be expected from CO adding to the pool of surface bound partial oxygenates but not being hydrogenated to the more reduced species present. CO is oxidised to CO_2 by these catalysts but the addition of CO_2 itself to the reaction feed had no effect on the formation of products (Supplementary Figure 25).

Discussion

Taking into account all of the experimental data presented in our study and insights from computational work it is possible to comment further on the likely mechanism by which the observed products are formed. The resulting scheme is illustrated in Fig. 6. C_1 and C_2 oxygenates are most likely formed in separate pathways from an initial, common, surface CH_3* species. Precursors for the observed methanol and methylhydroperoxide products are methoxy and methylperoxy species which we also consider to be surface bound. Given the high oxygen partial pressure present in the reaction, the initial activation of methane to form surface bound CH_3* will immediately establish an equilibrium with CH_3OO* on the catalyst surface. We estimate that the calculated TONs (*e.g.,* Table 1, entry 9, Supplementary Note 1) corresponds to 142 molecules per particle per second across around 2200 surface Au atoms, suggesting that

the surface coverage of CH_3OO^* and other metastable C_1 intermediates, such as CH_2O^* and CHO^*, will be too low for reactions between such species to be significant. This implies that self-reactions between these highly reactive intermediates, commonly described in gas phase chemistry, can be excluded.

For the C_2 oxygenates, acetic acid and peracetic acid, the analogous precursors are acyl (CH_3CO^*) acetoxy $(CH_3C(O)O^*)$ and acylperoxy $(CH_3C(O)OO^*)$. Ethane oxidation in our system mainly forms CO_2 (and some methane), and we find no ethane product during methane oxidation. These observations suggest that C_2 formation is not via coupling of CH_3^* with CH_3^*, and we propose that a surface bound acyl precursor (CH_3CO^*) is formed via a reaction of CH_3^* with surface bound CO^* (Figure 6). We consider that an equilibrium exists between acyl and acyl peroxy that is analogous to the CH_3^*/CH_3OO^* equilibrium.

The early formation of C_2 oxygenated products, actually before the appearance of C_1 oxygenates (Fig. 5c), suggests that a population of the precursors for C_2 formation appears very rapidly on the catalyst surface. However, the low selectivity to CO_2 throughout reaction shows that final oxidation of surface CO^* is very slow. Furthermore, desorption of CH_2O or CO is not observed in our experiments. Indeed, theoretical studies have shown that CO is very strongly bound on Au surfaces[Error! Reference source not found.,Error! Reference source not found.] and this is consistent with CO not being observed as a product. These oxidised surface intermediates, and we propose that chemisorbed CO^* dominates, then react with the flux of CH_3^* being formed by methane oxidation (or the reverse of CH_3OO^* formation (reaction 2)) to form acyl, acetoxy and acylperoxy and hence yield the observed C_2 oxygenate products.

[13]C labelling for the combined CH_4 and CO oxidation experiments (Supplementary Table 13) show that the methyl group of acetic acid comes mainly from CH_4 and that ^{13}C labelled CO in the gas phase is incorporated into the carbonyl group of the C_2 oxygenated products, but with substantially lower abundance. One would expect at least some formation of chemisorbed CO^* from gas phase CO, so these labelling experiments seem consistent with our proposal of carbon-carbon bond formation between CH_3^* and CO^* to give CH_3CO^*, as the route to C_2 products. The rather slow oxidation of CO in CO only experiments (Supplementary Table 12), and the absence of any observed CO product in methane oxidation, also suggest a substantial barrier to exchange between gas phase CO and CO^*.

The very rapid initial formation of C_2 oxygenates in H_2O as the solvent is followed by sustained production which remains a major reaction path (Fig. 5c). In contrast, methanol appears at a steadier rate throughout the reaction (Fig. 5b). In D_2O as the solvent, similar initial formation of C_2 oxygenates is observed (Fig. 5c), but then stops. These observations suggest an initial

state of the fresh catalyst (for example the presence of H^+, OH^* or H_2O^*) that enables rapid reaction of methane to form the distribution of surface C_1 intermediates we have described above, as well as the formation and release of C_2 oxygenates. In H_2O solvent, key surface species are replenished and the formation and release of C_2 products continues, but at a somewhat slower rate. Since formation of C_1 and C_2 oxygenates compete for CH_3^*, this slowing of the C_2 formation rate may be why C_1 oxygenate formation then appears at a steady rate. In D_2O as solvent, the same initial state of the fresh catalyst again causes early formation of C_2 oxygenates, but the key surface species are no longer replenished and C_2 formation then stops. It should be noted that CO_2 formation continues in D_2O, at a somewhat higher rate than in H_2O (Fig. 5d), so the cascade of C_1 oxygenated species from CH_3^* to CO^* continues in both solvents. These combined observations suggest a key role for hydrogen containing surface species in enabling the formation and release of C_2 oxygenates, for example H^+, OH^* or H_2O^*. We consider that one possibility is that the carbon-carbon bond forming, reaction (7), is reversible.

$$CH_3^* + CO^* \rightleftharpoons CH_3CO^* \tag{7}$$

Then the fate of CO^* is governed by competition between reactions (8) and (9):

$$O^* + CO^* \longrightarrow CO_2 \tag{8}$$

$$CH_3CO^* \xrightarrow{\text{hydrolysis}} CH_3COOH \tag{9}$$
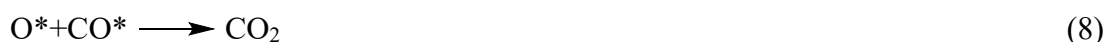
The hydrolysis step required to convert CH_3CO^* to acetic acid will be slower in D_2O than H_2O so that the competition for reversing the C-C bond formation and then losing CO^* by oxidation to CO_2 will reduce the rate of C_2 formation.

The main effect of adding CO to the methane oxidation system is to substantially increase the rate of methane oxidation and methanol formation (Table 1). We propose that this is due to CO maintaining the catalyst in a reduced state. There is an interesting secondary effect of added CO on the product distribution. Whereas the methanol yield increases by more than an order of magnitude, the methyl hydroperoxide yield becomes negligible. This may be due to the surface analogue of a known reaction[30] between CH_3OO and CO (equation (6)) which would switch products away from methyl hydroperoxide to methanol. In contrast to C_1 oxygenates, addition of CO increases C_2 oxygenate yield only modestly. This may be due to the rate of formation of C_2 products being lower on the reduced catalyst that will be present in the presence of CO; or could also be caused by a rapid reaction of CO with CH_3OO^* which will also impact the standing CH_3^* concentration via the reversible equilibrium between these two species. Hence, despite a large increase in the flux of CH_3^* formation, its standing concentration

increases only modestly, and the reaction of CH_3* with $CO*$ does not greatly change.

In conclusion, we have shown that Au nanoparticles supported on ZSM-5 can oxidise CH_4 to methanol and acetic acid with minimal formation of CO_2. Although comparison between batch and flow reactor conditions can only be qualitative it is possible to make some important considerations. We report, in our batch experiments ,a maximum oxygenate productivity at short times of 7.3 mol/mol$_{Au}$/h (37 mmol/g$_{Au}$/h) (Table 1, entry 10). Even at 1 h of reaction time a productivity of 1.9 mol/mol$_{Au}$/h (9.5 mmol/g$_{Au}$/h) is observed which is higher than that reported for Cu-based catalysts tested under similar conditions under flow conditions (Supplementary Table 2)[22,23]. In contrast to the Cu-zeolite catalysts previously reported for which only C_1 products are observed, C_2 oxygenates are the major products observed with the Au-ZSM-5 catalyst demonstrating that the Au catalyst operates by a different mechanism. Importantly, we observe this reaction in the absence of a co-reductant, and we show that the mechanism largely involves surface bound intermediates rather than species in the fluid phase.

Methods

Note on safe operation of experiments

Any reaction involving catalytic oxidation must take care to work under conditions outside of the explosive mixture composition of the reagents. In the case of methane with oxygen C M Cooper and P J Wiezevich have shown that as long as the experiments are conducted at $\leq 14\%$ O_2 even at elevated temperature and pressure the experiment is outside of the explosive regeme.[33] This is the case for all our experiments.

Catalyst Preparation. H-ZSM-5 zeolites with SiO_2/Al_2O_3 of 23, 25, 50 and 170 were obtained from Nankai University catalyst company Co., Ltd and Zeolyst International. H-ZSM-5 with SiO_2/Al_2O_3 of 25 was used as support for Au loading unless specified otherwise. Gold(III) chloride trihydrate ($HAuCl_4 \cdot 3H_2O$, $\geq 49.0\%$ Au basis) was purchased from Merck. SiO_2 (particle size: 30 nm) and γ-Al_2O_3 (particle size: 30 nm) were obtained from the Aladdin Chemical Reagent Co., Ltd. Aqueous ammonia (25-28 %), sodium carbonate (99.8%), sodium hydroxide ($\geq 96\%$) and hydrochloric acid (37%) were obtained from Sinopharm Chemical Reagent Co., Ltd. Methane (99.999%), ethane (99.9%) and carbon monoxide (99.999%) were obtained from Dalian Special Gases Co., Ltd. D_2O (^2H, 99.9%) was purchased from Qingdao Tenglong Weibo Technology Co., Ltd. Nitrogen (99.999%), oxygen (99.999%) and synthetic air (21% O_2 and 79% N_2) were obtained from Wuhan Huaxing Industrial Gas Co., Ltd. $^{13}CH_4$

(^{13}C, 99%) and ^{13}CO (^{13}C, 99%) was purchased from Cambridge Isotope Laboratories, Inc. All materials and reagents were used directly without purification.

Au loaded catalysts were prepared by a deposition-precipitation methodology using aqueous ammonia as the base to control the pH value. Typically, 3.0 g of zeolite/support dispersed in 200 ml of deionized water and a known amount of 6.0 mmol/L HAuCl$_4$ aqueous solution were mixed in a flat bottom beaker under stirring at 600 rpm. An appropriate amount of 2.5 wt.% aqueous ammonia solution was slowly dropped into the above solution until the expected pH value was achieved. This step took more than 30 min at room temperature. The resulting solution was aged in a pre-heated water bath at 60 ºC for 2 h under stirring at 600 rpm. Then, the sample was filtered and fully washed with deionized water. After drying in an oven at 60 ºC overnight, the sample was further calcined in a tubular furnace in static air. The temperature was programmed from room temperature to 240 ºC at 3 ºC/min and kept at 240 ºC for 90 min, and then cooled to room temperature.

Catalyst Characterization. XRD patterns were recorded on a Panalytical X' Pert PRO X-ray diffractometer (40 kV, 40 mA) using Cu Kα (λ=1.5406 Å) radiation with scan rate 0.2° s^{-1}. The Au4f XPS spectra were collected using a Thermo Fisher Scientific K-Alpha spectrometer using an Al Kα source with pass energy 150.0 eV. The photoelectron peak of C1s, located at 284.8 eV, was used as reference for binding energies in all XPS spectra. BET surface area was obtained by nitrogen isotherms at -196 °C using a Micromeritics ASAP 2020 M system. Samples were outgassed for 10 h at 200 °C before the measurements. Au and Fe content in the catalysts was determined by inductively coupled plasma Optical Emission Spectrometry (ICP-OES) with an Agilent 700 spectrometer. The Au/ZSM-5 catalysts were structurally characterized using a combination of scanning electron microscopy (SEM), transmission electron microscopy (TEM) and scanning transmission electron microscopy (STEM). SEM back-scattered electron (BSE) imaging was carried out at Cardiff University on a TESCAN MAIA3 microscope equipped with a Schottky gun operating at 30 kV. Samples for TEM and STEM analysis were dry mounted onto holey carbon film TEM grids. TEM bright field (BF) imaging experiments were carried out at Cardiff University using a JEOL 2100 microscope equipped with a LaB$_6$ electron gun operating at 200 kV. Particle size distributions were determined from these BF-TEM images using ImageJ in which a minimum of 300 particles were counted for each specimen. STEM high angle annular dark field (HAADF) imaging was performed at the National University of Singapore, using an aberration-corrected JEOL ARM200CF microscope equipped with a cold field-emission gun operating at 200 kV. ^{27}Al MAS NMR experiments were carried out at 9.4 T on a Bruker Avance III 400 spectrometer

with a 4 mm double-resonance probe. The resonance frequency was 104.05 MHz for ^{27}Al. The spectra were acquired by small-flip angle technique with a pulse length of 0.2 μs (corresponding to a π/18 flip angle) and a recycle of delay of 1s. The ^{27}Al chemical shifts were referenced to 1M $Al(NO_3)_3$ aqueous solution (0 ppm). The magic angle spinning rate was set to 10 kHz.

Catalyst Testing. Methane oxidation with oxygen was carried out in a 25 mL stainless steel Parr autoclave reactor. In general, 0.1 g catalyst and 15 mL deionized water were transferred into the reactor and the reactor was sealed and bubbled with pure nitrogen for more than 30 min to remove dissolved gas. After purging three times with methane, the reactor was pressurized with a gas mixture of methane and oxygen. The total pressure was set at 24.2 bar with varied methane and oxygen (0.14~3.5 bar) partial pressures measured at room temperature. The mixture was initially stirred at 1000 rpm for 10 min at room temperature and the pressure stayed constant at around 24 bar. The reactor was then heated to the desired reaction temperature (120-240 ºC) within 30 min and maintained at the reaction temperature for 5 min to 2 h. The reaction was stopped by cooling in ice water to a temperature below 10 ºC in order to minimize the loss of volatile products. Gas in the head space of the reactor was collected for analysis in a gas sampling bag at the end of a reaction. Liquid products were sampled using a glass syringe with Teflon filter head for NMR analysis. Heavy water was used in place of water as the solvent and the reactions were performed at the same condition to that using water as solvent.

Methane oxidation using synthetic air as oxidant was performed with the same procedure. Air partial pressure in the reaction varied from 0.67 to 4.2 bar and the total pressure was balanced to be 24.2 bar with methane. The reaction was performed at 240 ºC for times as reported.

For reactions of methane, oxygen and CO (or CO_2), various oxygen and CO (CO_2) partial pressures (0 to 2.5 bar) were used and the total pressure was balanced to be 24.2 with methane. Generally, the reaction was performed at 240 ºC for 1-4 h.

Ethane was compared with methane for the oxidation reactions under the same conditions.

To test the role of methanol in the reaction mechanism methanol solution with the conditions specified in Supplementary Fig. 23.

Reactions in D_2O solvents were carried out at a series of temperatures from 120 ºC to 240 ºC using the standard experimental procedure and gas composition described above (Supplementary Table 10) for catalysts with 0.5 wt.% Au loading.

Isotopic tracer experiments. To trace the fate of carbon atoms from methane, CH_4 with 6%

^{13}C-labeled mixed with 94% in natural abundance was used in the co-reaction with oxygen and CO. The reactions were performed at 240 ºC for 1 or 4 h with initial partial pressure of 20.7 bar, 1.0 bar and 2.5 bar for CH_4, O_2 and CO respectively (Gases charged to the autoclave at room temperature). CO (6% ^{13}C-labeled mixed with 94% in natural abundance) was alternatively used to trace the fate of carbon atom from CO in the co-reactions under the same conditions.

A high-sensitivity NMR CryoProbe on a Bruker Avance-600 liquid NMR spectrometer was employed to analyze the liquid products obtained from the isotopic tracing experiments. ^{1}H NMR spectra were recorded using a water suppression pulse sequence. ^{1}H-^{13}C heteronuclear multiple-bond correlation (HMBC) experiments were performed for the analysis of ^{13}C labelling in methanol and acetic acid.

In the ^{1}H NMR spectra (Supplementary Fig. 24a), the protons attached to methyl groups of methanol and acetic acid produce doublet due to the spin-spin splitting by enriched ^{13}C atom. The integral of the doublet shows the abundance of the ^{13}C atom in the methyl group. Together with the ^{1}H-^{13}C HMBC spectra (Supplementary Fig. 24b), the abundance of ^{13}C atom on carbonyl group of acetic acid can be obtained. The details are shown in Supplementary Table 13.

Time on-line measurements. The reaction yields were measured for a series of reaction times to build up a picture of the evolution of products as the reaction proceeds in both H_2O and D_2O solvents (Fig. 5, Supplementary Fig. 21, Supplementary Table 11). For these experiments, the reaction temperature was lowered to 200 °C in order to ensure good resolution of the kinetic curves at short reaction times. The gas mixture was also altered to CH_4 (20.7 bar), O_2 (1 bar) with N_2 at (2.5 bar) added to maintain a total gas pressure consistent with earlier experiments. The reactor design used here with significant gas pressure in the autoclave headspace means that the time online data of Fig. 5, Supplementary Fig. 21, Supplementary Table 11 did come not from a sampling procedure but from collections of single experiments for each point. To achieve this fresh catalyst samples were used in the reactor for each time point recorded and so we expect that trends are thus more reliable than individual data points.

Product analysis. The gaseous products analysis was performed on a Shimadzu GC-2014C Gas chromatography system equipped with a methanizer-unit and FID detector using a TDX-01 packed column. The liquid products were quantified by ^{1}H NMR on a Bruker Avance-600 liquid NMR spectrometer using a water suppression pulse sequence (Watergate5).[34] The measurement was calibrated using an external standard method with a series of methanol solutions with known concentrations. The experimental error bounds were determined as ±5%.

Typically, 0.4 mL of liquor after reaction was mixed with 0.1 mL of heavy water to prepare a solution for NMR measurement. The concentration (mmol/L) of each liquid product was determined based on the calibration plot (Supplementary Fig. 4).

The dissolved CO_2 in reaction solution was analysed with the headspace sampling method on GC proposed by Sarradin and Caprais.[35] A 25 mL gas-tight syringe with seal valve was used in place of headspace flask. Typically, 10 ml of the fresh reaction solution (the catalyst still present) and 0.1 mL of hydrochloric acid (6 mol/L) was quickly taken into the syringe under a nitrogen atmosphere. Then the syringe was filled with nitrogen to a volume of 20 mL. After that, the syringe was heated for 30 min at 70 °C and shaken for 30 seconds. This operation was repeated several times in order to completely extract CO_2. The gas in the syringe was analysed on a Shimadzu GC-2014C Gas Chromatography system equipped with a methanizer-unit and FID detector using a TDX-01 packed column. The productivity of CO_2 was calibrated by standard gas. The results for a standard reaction are shown in Supplementary Table 14 and show that only minimal CO_2 was dissolved in the water used in the reaction. To estimate the error in measured productivity four repeat experiments were performed giving a standard deviation of between 9 and 12 % (Supplementary Table 15).

Electronic Structure Calculations. All calculations were performed using the Vienna Ab initio Simulation Package (VASP)[36,37] with the generalized gradient approximation (GGA) functional of Perdew, Burke and Ernzerhof (PBE).[38] Grimme D3 level dispersion[39] was also included to account for attractive van der Waals forces between adsorbates and surfaces. All calculations were carried out spin unrestricted unless otherwise stated. The Projector Augmented Wave method (PAW) was used for core states.[40,41] For gold this means that there are 60 core electrons represented by PAW and the states for 19 valence electrons are calculated explicitly. All geometry relaxations on the nanoparticle system were performed with electronic and geometric convergence criteria set to 10^{-6} eV and 0.01 eV Å^{-1} or lower, respectively, calculations on the extra framework cationic system used a 10^{-5} eV electronic cut-off.

For reaction barriers, initial estimates of the transition state were made from the minimum energy path between reactants and products using a either the Nudged Elastic Band (NEB)[42] method or with atom distance constraints for bonds breaking/forming in a given elementary steps implemented within the Atomic Simulation Environment (ASE).[43] NEB barriers were usually refined with the climbing image modification developed by Henkelmen and co-workers.[44,45] We use between 5 and 10 images in NEB calculations with the initial interpolation carried out using linear interpolation for diatomic dissociation and a group centred interpolation approach[46] for more complex cases. In the constrained optimisation method with ASE a

particular atom-atom distance (C..H or O..H) was incremented using an initial step size of 0.2 Å to identify the region of the saddle point and at each step the system was optimized to a level of 0.05 eV Å^{-1} under the imposed constraint before the next atom..atom distance increment took place. This region was then further refined using a step size of 0.03 Å. NEB or bond scan transition state estimates were used for transition state optimisation using the dimer method[44] with a geometry convergence of 0.05 eV Å^{-1}. Transition states were verified by performing a frequency calculation on the proposed transition state and confirming a single imaginary mode. Three classes of model were constructed to represent the Au species that could be present in the active catalyst are shown in Supplementary Fig. 15. Electron microscopy images show rounded particle morphologies (Supplementary Fig. 10) and particle size distributions (Supplementary Fig. 12) show that Au is present exclusively as relatively large nanoparticles with average particle sizes of 8.1 nm for fresh materials and 14.1 nm for used catalysts. To model the surfaces of these particles periodic slab calculations were used for the flat Au(111) and Au(100) planes. To represent the irregular surface features of the rounded particles a stepped surface model was also constructed by removing rows of atoms from the Au(100) slab to give steps with (111) edges (Supplementary Fig. 15a). The Au(111) and Au(100) slab models were generated by cleaving the optimised bulk fcc unit cell. In both cases, 5 atomic layers were used and supercells in the surface vectors consisting of a (2×2) expansion for the (111) slab and a (3×3) expansion for the (100) case so that the number of atoms in the (111) and (100) slabs was set to 80 and 90 atoms respectively. A vacuum gap of 13 Å was employed and the bottom three layers of each slab were fixed at their optimised bulk co-ordinates. The plane wave cut off for slab calculations was set to 400 eV based on convergence of the bulk unit cell energy. A dipole correction along the z-direction of the slab, perpendicular to the exposed surface, was included in all calculations. For the original optimisation of the bulk structure *k*-point sampling of 7×7×7 was used. The larger unit cells of the slab calculations allowed this to be reduced to 3×3×1. For the Au cation system, no vacuum gap was required as all important surfaces were internal.

It is also possible that, under reaction conditions, the particles seen in electron microscopy could act as reservoirs for smaller nanoparticles or even for ion exchange of Au cations into the zeolite pore structure. Accordingly, we also considered the ability of sub-nanometer metal particles (Supplementary Fig. 15b) and extra-framework Au cations (Supplementary Fig. 15c) to act as catalytic sites for the activation of oxygen and methane.

The sub-nanometer Au particles contained 38 atoms in a truncated octahedral geometry (Supplementary Fig. 15b) were placed within a cubic periodic box with edges of 25 Å. A plane

wave cut-off of 500 eV was found to be sufficient to converge the total energy of Au_{38} nanoparticles to less than 0.008 eV. For these isolated nanoparticles only the Γ-point is needed in reciprocal space (k-point grid sampling 1×1×1). For the Au_{38} particles Gaussian smearing with a very small width of 0.001 was employed to represent the discrete nature of the states within the particle. For all geometry relaxation calculations, all atoms of adsorbate and clusters were free to move with no atomic restraints applied.

To represent Au acting as an extra-framework cation in the ZSM-5 framework, the model shown in Supplementary Fig. 15c was constructed. Here, a single tetrahedral site in a purely SiO_4 MFI framework (the structure of ZSM-5) is substituted with aluminum at the T12 site to give the extra-framework Au cation a formal oxidation state of +1 situated near to the junction of the straight and sinusoidal channel. A k-point mesh of 3×3×3 was used for optimization and transition state calculations for the resulting Au^+/ZSM-5 model.

The energy, E, as used in the various potential energy diagram figures, for molecular species was calculated as:

$$E = E_{cl+m} - E_{cl} - E_m \quad\quad\quad (10)$$

Where, E_{cl+m}, is the calculated total energy for the optimised active site model (slab, cluster or Au^+/ZSM-5) model with the adsorbate in a given location, E_{cl}, is the calculated total energy for the optimised cluster or slab alone and E_m, is the calculated total energy for the optimised molecule alone, effectively in the gas phase. All three calculations employ the same periodic simulation cell and calculation parameters as defined above. For multiple adsorbates, *e.g.* O_2 and CH_4, potential energy diagrams were produced based on the stable gas phase species and the relevant clean cluster, surface or empty Au^+/ZSM-5 zeolite. The oxygen reference was always taken as the triplet ground state of the O_2 molecule.

Data Availability

All data used in this publication is available free of charge from Cardiff University via http://doi.org/10.17035/d.2021.0142278187 or available from the authors upon reasonable request.

Author Contributions

J.X. and G.J.H conceived the research idea and organized the research programs. G.Q. and R.J.L. prepared catalyst samples, G. Q., X.Z. and F.D. performed the catalytic experiments and

NMR analysis, T.E.D, Q.H., A.G.R.H. obtained electron microscopy data under the direction of C.J.K.. D.J.W., A.N, M.A.S. and M.Q. carried out most of the computational chemistry calculations. D.B. and M.J.H. provided mechanistic interpretation of results along with C.R.A.C and D.J.W. who integrated experimental and computational insights. B.A.M. and B.H. provided advice on the industrial context of the work. J.X., G.J.H. and D.J.W. wrote the paper and all authors discussed the results and the various revisions of the manuscript. J.X. and G.J.H. contributed equally to this work.

Competing Interests

The authors declare no competing interests.

References

1. Hammer, G. et al. *Natural Gas in Ullmann's Encyclopaedia of Industrial Chemistry.* (Wiley-VCH, Weinheim, 2012).

2. Gesser, H. D., Hunter, N. R. & Prakash, C. B. The direct conversion of methane to methanol by controlled oxidation. *Chem Rev.* **85**, 235-244 (1985).

3. Conley, B. L. et al. Design and study of homogenous catalysts for the selective, low temperature oxidation of hydrocarbons. *J. Mol. Cat. A: Chem.* **251**, 8-23 (2006).

4. Hargreaves, J. S. J., Hutchings, G. J. & Joyner, R. W. Control of product selectivity in the partial oxidation of methane. *Nature*, **348** 428-429 (1990).

5. Periana, R. A. et al. A mercury-catalyzed, high-yield system for the oxidation of methane to methanol. *Science* **259**, 340-343 (1993).

6. Periana, R. A. et al. Platinum catalysts for the high-yield oxidation of methane to a methanol derivative. *Science* **280**, 560-564 (1998).

7. Sobolev, V. I., Dubkov, K. A., Panna, O. V. & Panov, G. I. Selective oxidation of methane to methanol on a FeZSM-5 surface. *Catal. Today* **24**, 251-252 (1995).

8. Starokon, E. V. et al. Oxidation of methane to methanol on the surface of FeZSM-5 zeolite. *J. Catal.* **300**, 47-54 (2013).

9. Starokon, E. V., Parfenov, M. V., Pirutko, L. V., Abornev, S. I. & Panov, G. I. Room-temperature oxidation of methane by α-oxygen and extraction of products from the FeZSM-5 surface. *J. Phys. Chem. C* **115**, 2155-2161 (2011).

10. Parfenov, M. V., Starokon, E. V., Pirutko, L. V. & Panov, G. I. Quasicatalytic and catalytic oxidation of methane to methanol by nitrous oxide over FeZSM-5 zeolite. *J. Catal*. **318**, 14-21 (2014).

11. Hammond, C. et al. Direct catalytic conversion of methane to methanol in an aqueous medium by using copper-promoted Fe-ZSM-5. *Angew. Chem. Intl. Ed.* **51**, 5129-5133 (2012).

12. Yu, T. *et al.* Highly Selective Oxidation of Methane into Methanol over Cu-Promoted Monomeric Fe/ZSM-5. *ACS Catal.* **11**, 6684-6691 (2021).

13. Narsimhan, K et al. Methane to acetic acid over Cu-exchanged zeolites: mechanistic insights from a site-specific carbonylation reaction. *J. Am. Chem. Soc.* **137**, 1825-1832 (2015).

14. Shan, J., Li, M., Allard, L. F., Lee, S. & Flytzani-Stephanopoulos, M. Mild oxidation of methane to methanol or acetic acid on supported isolated rhodium catalysts, *Nature*,

551, 605-608 (2017).

15. Tang, Y. et al. Single rhodium atoms anchored in micropores for efficient transformation of methane under mild conditions, *Nature Commun.* **9**, 1231 (2018).

16. Jin, Z. et al. Hydrophobic zeolite modification for in situ peroxide formation in methane oxidation to methanol, *Science* **367**, 193-197 (2020).

17. Agarwal, N. et al. Aqueous Au-Pd colloids catalyze selective CH_4 oxidation to CH_3OH with O_2 under mild conditions. *Science* **358**, 223-226 (2017).

18. Groothaert, M. H., Smeets, P. J., Sels, B. F., Jacobs, P. A. & Schoonheydt, R. A. Selective oxidation of methane by the bis(μ-oxo)dicopper core stabilized on ZSM-5 and mordenite zeolites. *J. Am. Chem. Soc.* **127**, 1394-1395 (2005).

19. Patrick, T. et al. Isothermal cyclic conversion of methane into methanol over copper-exchanged zeolite at low temperature. *Angew. Chem. Intl. Ed.* **55**, 5467-5471 (2016).

20. Grundner, S. et al. Single-site trinuclear copper oxygen clusters in mordenite for selective conversion of methane to methanol. *Nature Comm.* **6**, 7546 (2015).

21. Sushkevich, V. L., Palagin, D., Ranocchiari, M. & van Bokhoven, J. A. Selective anaerobic oxidation of methane enables direct synthesis of methanol. *Science* **356**, 523-527 (2017).

22. Narsimhan, K., Iyoki, K., Dinh, K. & Román-Leshkov, Y. Catalytic oxidation of methane into methanol over copper-exchanged zeolites with oxygen at low temperature. *ACS Central Sci*. **2**, 424-429 (2016).

23. Dinh, K.T., Sullivan, M.M., Narsimhan, K., Serna, P., Meyer, R.J., Dinca, M. Roman-Leshkov, Y. Continuous partial oxidation of methane to methanol catalyzed by diffusion-paired copper dimers in copper-exchanged zeolites. *J. Amer. Chem. Soc*. **141**, 11641−11650 (2019).

24. Koishybay, A. & Shantz, D.F., Water is the oxygen source for methanol produced in partial oxidation of methane in a flow reactor over Cu-SSZ-13. *J. Amer. Chem. Soc*. **142**, 11962−11966 (2020).

25. Sarv, P. et al., Mobility of the acidic proton in Brønsted sites of H-Y, H-Mordenite, and H-ZSM-5 Zeolites, studied by high-temperature ^{1}H MAS NMR. *J. Phys. Chem*., **99**, 13763-13768 (1995).

26. Herzing, A. A, Kiely, C. J., Carley, A. F., Landon, P. & Hutchings, G. J. Identification of active gold nanoclusters on iron oxide supports for CO oxidation. *Science*. **321**, 1331–1335 (2008).

27.   He, Q. et al. Population and hierarchy of active species in gold iron oxide catalysts for carbon monoxide oxidation. *Nat. Commun.* **7**, 12905 (2016).

28.   Jin, R. et al. Low temperature oxidation of ethane to oxygenates by oxygen over iridium-cluster catalysts. *J. Am. Chem. Soc.* **141**, 18921-18925 (2019).

29.   Gouget, A. et al. Increased dispersion of supported gold during methanol carbonylation. *J. Am. Chem. Soc.* **131**, 6973-6975 (2009).

30.   Denisov, E. T. & Shestakov, A. F. Reactions of Alkoxy and Peroxy Radicals with Carbon Monoxide. *Kinet. Catal.*, **49**, 1–10 (2008).

31.   Boronat, M., Concepción, P. & Corma, A. Unravelling the Nature of Gold Surface Sites by Combining IR Spectroscopy and DFT Calculations. Implications in Catalysis. *J. Phys. Chem. C* **113**, 16772-16784 (2009).

32.   Liu, Z-P., Hu, P. & Alavi, A., Catalytic Role of Gold in Gold-Based Catalysts: A Density Functional Theory Study on the CO Oxidation on Gold. *J. Amer. Chem. Soc.* **124**, 14770−14779 (2002).

33.   Cooper, C. M. & Wiezevich, P. J. Effects of Temperature and Pressure on the Upper Explosive Limit of Methane-Oxygen Mixtures. *Ind. Eng. Chem.* **21**, 1210–1214 (1929).

34.   Liu, M. *et al.* Improved WATERGATE Pulse Sequences for Solvent Suppression in NMR Spectroscopy. *J. Magn. Reson.* **132**, 125–129 (1998).

35.   Sarradin, P.-M. & Caprais, J.-C. Analysis of dissolved gases by headspace sampling gas chromatography with column and detector switching. Preliminary results. *Anal. Commun.* **33**, 371-373 (1996).

36.   Kresse, G. & Hafner, J. *Ab initio* molecular dynamics for liquid metals. *Phys. Rev. B* **47**, 558–561 (1993).

37.   Kresse, G. & Furthmüller, J. Efficient iterative schemes for *ab initio* total-energy calculations using a plane-wave basis set. *Phys. Rev. B* **54**, 11169–11186 (1996).

38.   Perdew, J. P., Burke, K. & Ernzerhof, M. Generalized Gradient Approximation Made Simple. *Phys. Rev. Lett.* **77**, 3865–3868 (1996).

39.   Grimme, S., Antony, J., Ehrlich, S. & Krieg, H. A consistent and accurate *ab initio* parametrization of density functional dispersion correction (DFT-D) for the 94 elements H-Pu. *J. Chem. Phys.* **132**, 154104 (2010).

40.   Kresse, G. & Joubert, D. From ultrasoft pseudopotentials to the projector augmented-wave method. *Phys. Rev. B* **59**, 1758–1775 (1999).

41.   Blöchl, P. E. Projector augmented-wave method. *Phys. Rev. B* **50**, 17953–17979 (1994).

42.   Mills, G., Jónsson, H. & Schenter, G. K. Reversible work transition state theory: Application to dissociative adsorption of hydrogen. *Surf. Sci.* **324**, 305-337 (1995).

43.   Hjorth Larsen, A. *et al.* The atomic simulation environment—a Python library for working with atoms. *J. Phys. Condens. Matter* **29**, 273002 (2017).

44.   Henkelman, G. & Jónsson, H. A dimer method for finding saddle points on high dimensional potential surfaces using only first derivatives. *J. Chem. Phys.* **111**, 7010–7022 (1999).

45.   Kästner, J. & Sherwood, P. Superlinearly converging dimer method for transition state search. *J. Chem. Phys.* **128**, 014106 (2008).

46.   Thetford, A., Hutchings, G. J., Taylor, S. H. & Willock, D. J. The decomposition of H_2O_2 over the components of Au/TiO_2 catalysts. *Proc. R. Soc. Math. Phys. Eng. Sci.* **467**, 1885–1899 (2011).
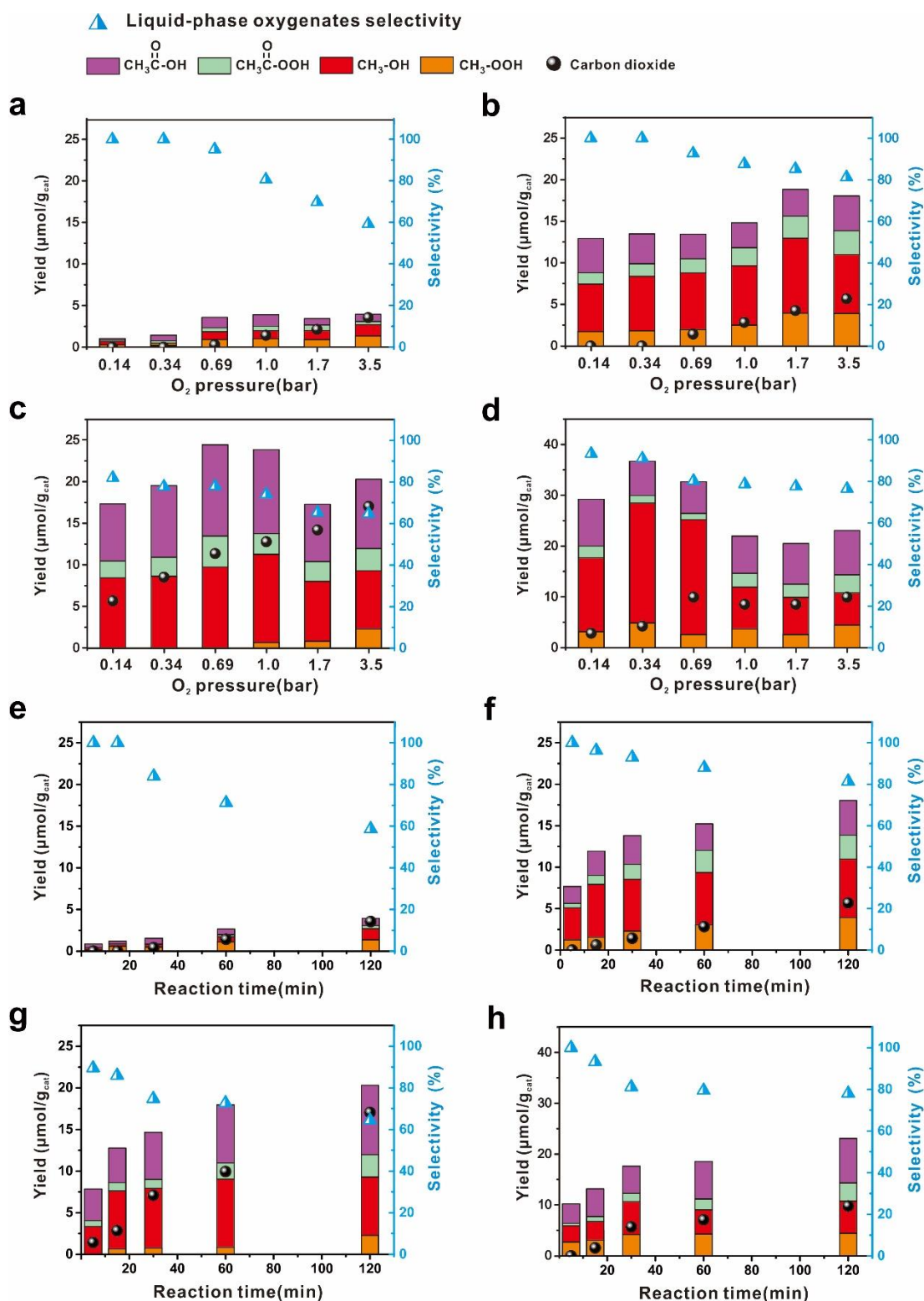
Fig. 1 Catalytic performance of Au/ZSM-5 catalysts for methane oxidation. a-d, The effect of O_2 partial pressure on the reaction at a total pressure of 24.2 bar ($CH_4 + O_2$) and reaction time of 120 min. **e-h**, The effect of reaction time on the reaction with CH_4 (20.7 bar) and O_2 (3.5 bar). **a**, **e** 0.12 wt.% Au, **b**, **f** 0.25 wt.% Au, **c**, **g** 0.5 wt.% Au, and **d**, **h** 1.0 wt.% Au. For all the reactions: catalyst (0.1 g), 240 °C, H_2O (15 mL).
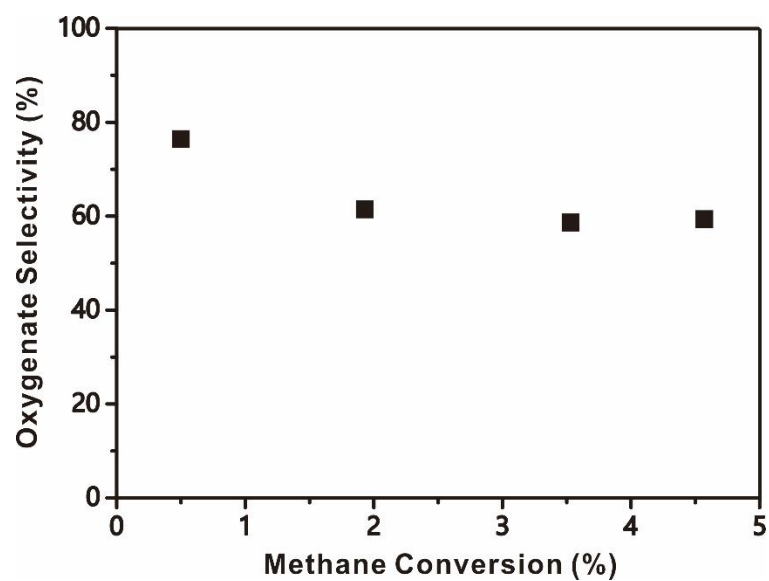
Fig. **2 Oxygenate selectivity as a function of methane conversion.** Reaction conditions (Supplementary Table 7): 0.5 wt.% Au/ZSM-5 catalyst (0.10 g), 240 °C, H_2O (15 mL), methane reacted with air with total pressure 24.2 bar using nitrogen.
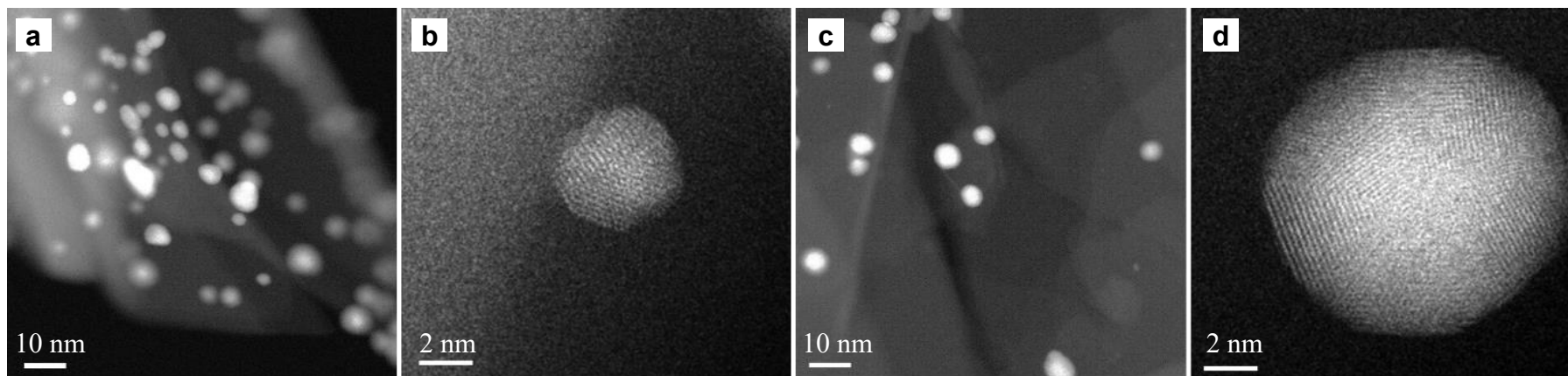
Fig. 3 STEM-HAADF images of 0.5 wt.% Au/ZSM-5 catalysts. a, b, fresh catalyst, and **c, d**, used catalyst after 2 h of methane oxidation reaction (23.2 bar CH_4, 1.0 bar O_2, 240 °C).
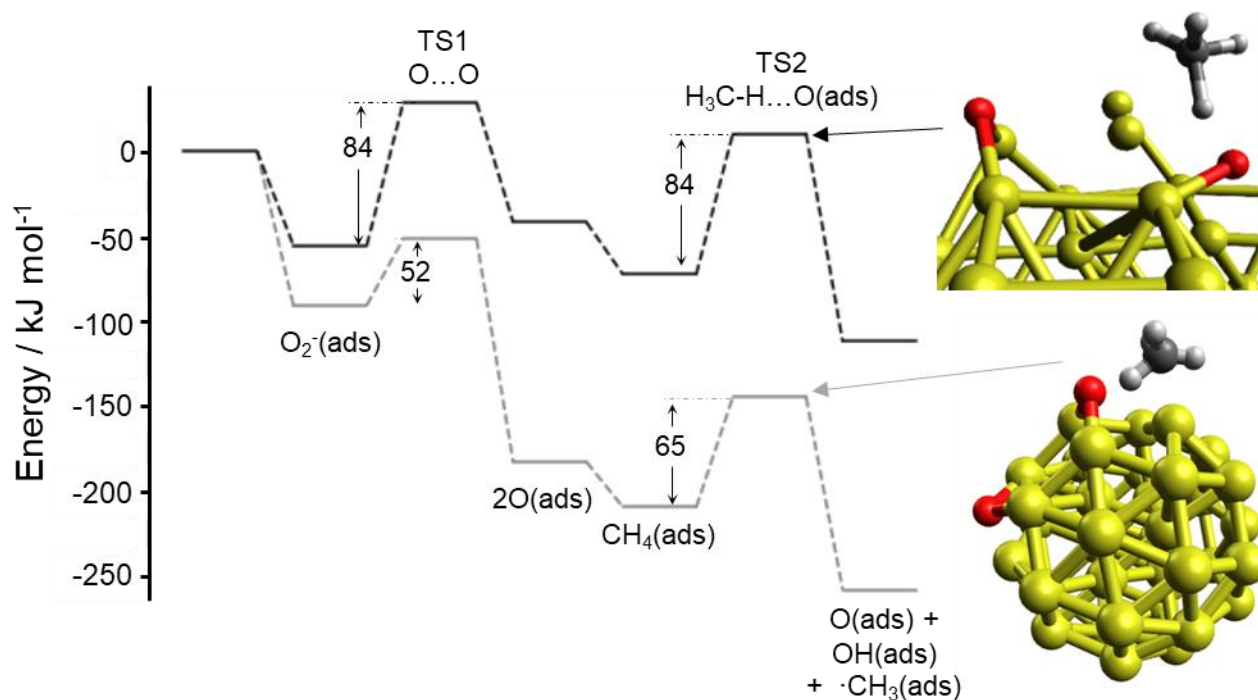
Fig. 4 Calculated reaction pathways for methane activation by surface O atoms. The zero of energy is for the clean surface, $O_2(g)$ and $CH_4(g)$ barrier heights are given in kJ mol^{-1} with TS1 representing dissociation of $O_2(ads)$ and TS2 the activation of a methane H_3C-H bond to form surface bound OH and CH_3 species. Energy values based on total calculated energy at PBE+D3 level without correction for vibrational contributions. Black lines are for the slab model of the Au(100) with (111) step edges, grey lines are for the Au_{38} nanoparticle. Graphical images show the structures of TS2 with atom colours: Au; yellow, O; red, C; grey and H; white.
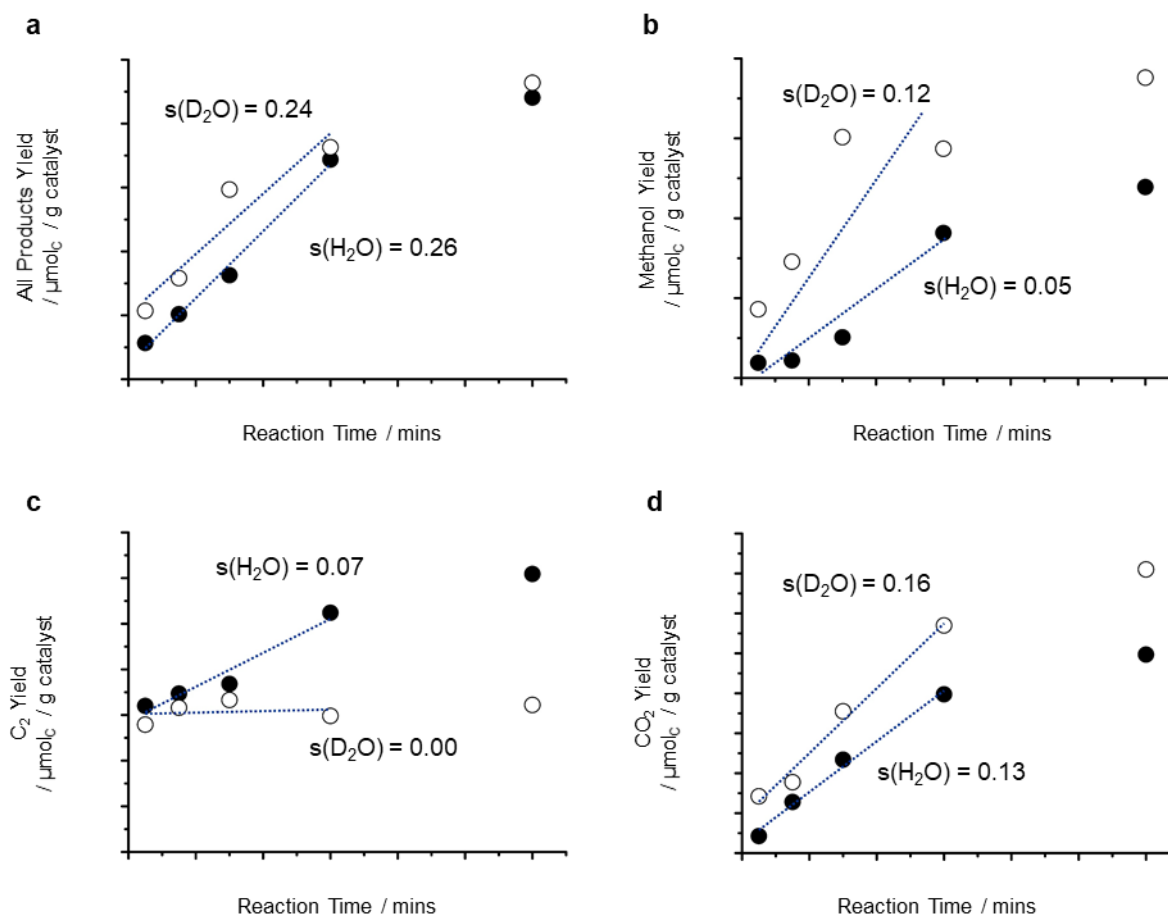
Fig. 5 Yield of products as a function of time. In all cases data for H_2O solvent is shown with filled symbols and that for D_2O solvent with open symbols. Dotted lines show least squares linear fits to the first 60 min of data with the initial gradient shown (s(H/D_2O)) in units of μmol_C g_{cat}^{-1} min^{-1} these slopes are proportional to the effective rate constants and so are used to calculate the k_H/k_D values discussed in the text. **a**, All products. **b**, Methanol yield. **c**, C_2 product yield. **d**, CO_2 yield. Reaction conditions: catalyst (0.1 g), H_2O/D_2O (15 mL), CH_4 (20.7 bar), O_2 (1.0 bar), N_2 (2.5 bar), 0.5 wt.% Au loading, reaction temperature (200 °C). All product yields are calculated as micromoles of carbon (μmol_C).
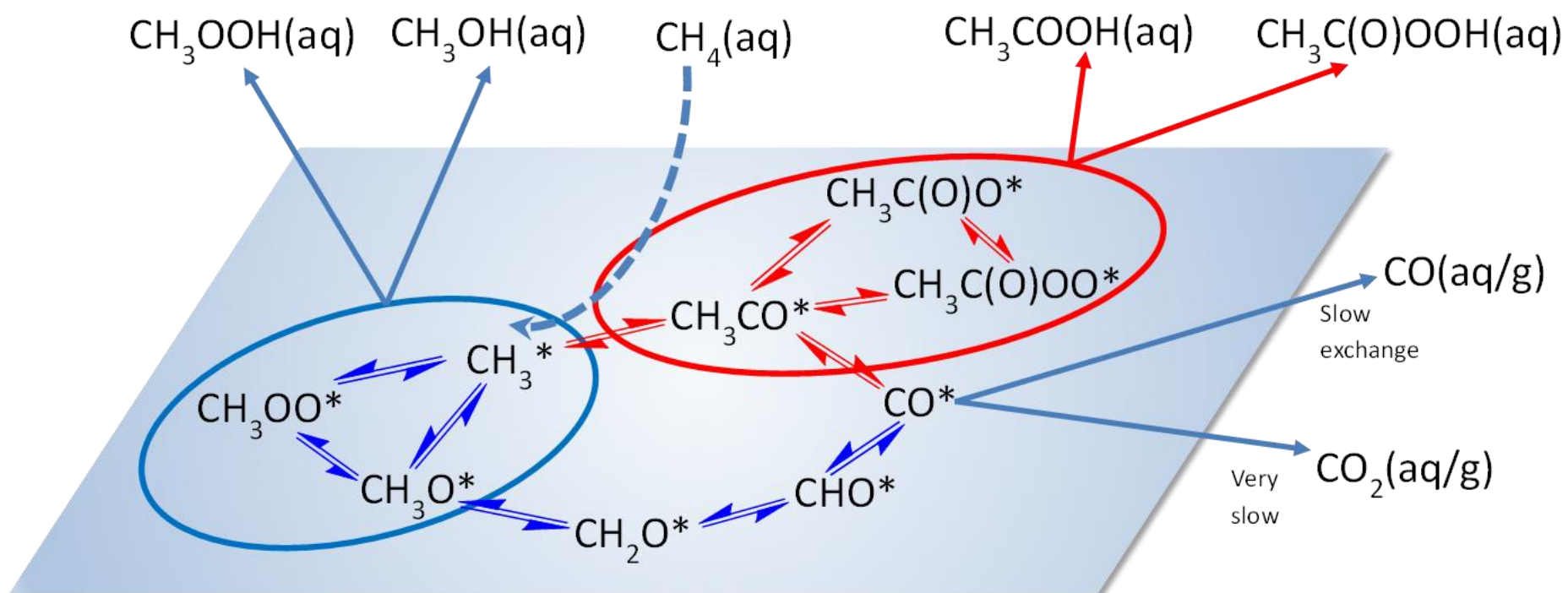
Fig. 6 Schematic illustration of the proposed surface catalysed reactions. Blue arrows and lines are used for C_1 intermediates and products, red arrows and lines are used for C_2 intermediates and products. The phase of each product is indicated as (aq): aqueous or (aq/g): partitioned between aqueous and gas phase surface species are labelled with "*". The surface species in blue/red ellipses lead to observed partial oxidation products through hydrolysis or hydrogen transfer.

Table 1 Catalytic performance of Au/ZSM-5 catalysts for the partial oxidation of methane.

Entry	Catalyst	Reactants CH_4, O_2, CO (bar)[a]	T (°C)	Time	Productivity (µmol/g_{cat})					Oxygenate Selectivity (%)	Oxygenate Productivity (µmol/g_{cat})
					Methanol	Methyl hydroperoxide	Acetic acid	Peracetic acid	CO_2		
1	H-ZSM-5	20.7, 3.5, 0	240	2 h	1.18	0.38	2.62	0.68	2.34	77.7	4.86
2	Au/SiO$_2$	20.7, 3.5, 0	240	2 h	0.10	0.04	0.78	0.18	1.44	58.9	1.10
3	Au/Al$_2$O$_3$	20.7, 3.5, 0	240	2 h	3.38	0.00	1.26	0.50	3.26	67.9	5.14
4	Au/ZSM-5	20.7, 3.5, 0	240	2 h	7.01	2.28	8.32	2.69	17.3	64.4	20.3
5	Au/ZSM-5	23.2, 1.0, 0	240	2 h	10.6	0.66	10.1	2.54	12.8	74.1	23.9
6	Au/ZSM-5	23.2, 1.0, 0	240	1 h	11.1	1.80	8.07	2.66	12.8	72.9	23.7
7	Au/ZSM-5	24.06, 0.14, 0	240	2 h	8.43	0.00	6.85	2.04	5.69	82.2	17.3
8	Au/ZSM-5-0.25[b]	24.06, 0.14, 0	240	2 h	5.70	1.74	4.11	1.36	b.d.[c]	100	12.9
9	Au/ZSM-5	20.7, 3.5, 0	240	5 min	3.34	0.00	3.79	0.70	1.42	89.7	7.83
10	Au/ZSM-5-0.25[b]	20.7, 3.5, 0	240	5 min	3.86	1.23	2.05	0.55	b.d.[c]	100	7.69[d]
11	Au/ZSM-5	20.7, 1.0, 2.5	240	1 h	136	0.00	19.9	4.64	n.d.[e]	n.d.[e]	161
12	Au/ZSM-5	20.7, 1.0, 2.5	240	4 h	545	0.00	79.0	2.36	n.d.[e]	n.d.[e]	627

Reaction conditions: catalyst 0.5 wt.% Au/ZSM-5 (0.10 g), water (15 mL)
[a]Gas pressures measured at room temperature prior to reaction; [b]Au loading is 0.25 wt.%; [c]below detection limit; [d]7.3 mol/mol$_{Au}$/h (37 mmol/g_{Au}/h) at 5 min reaction time, [e]not determined.